HHS Public Access
Author manuscript
IEEE Trans Med Robot Bionics. Author manuscript; available in PMC 2026 June 25.

Published in final edited form as:
IEEE Trans Med Robot Bionics. 2025 August ; 7(3): 1029–1040. doi:10.1109/tmrb.2025.3583160.

Serially-Connected Soft Continuum Robots for Endovascular Emergencies

Aedan Mangan[1], **Sukjun Kim**[1], **Noah Jones**[1], **Michael G. Brandel**[2], **Jeremy J. Heit**[3], **Alexander Norbash**[4], **John T. Hwang**[1], **Elliot Hawkes**[5], **Tania K. Morimoto**[1,6]

[1]Department of Mechanical and Aerospace Engineering, University of California San Diego, San Diego, CA 92093, USA

[2]Department of Neurosurgery, University of California San Diego, School of Medicine, San Diego, CA 92093, USA

[3]Departments of Radiology and Neurosurgery, Stanford University, Stanford, CA 94305, USA

[4]School of Medicine, University of Missouri-Kansas City, Kansas City, MO 64110, USA

[5]Department of Mechanical Engineering, University of California Santa Barbara, Santa Barbara, CA 93106, USA

[6]Department of Surgery, University of California San Diego, San Diego, CA 92093, USA

Abstract

Endovascular surgeries generally rely on push-based catheters and guidewires, which require significant training to master and can still result in high stress being exerted on the anatomy, especially in tortuous paths. Because these procedures are so technically challenging to perform, many patients have limited access to high-quality treatment. Although various robotic systems have been developed to enhance navigation capabilities, they can also apply high stresses due to sliding against the vascular walls, impeding movement and raising the risk of vascular damage. Soft growing robots offer a promising alternative since their method of movement via eversion minimizes interaction forces with the environment and enables follow-the-leader navigation through tortuous paths. However, reliable steering of small-scale growing robots remains a significant challenge. We propose a robot architecture that combines a hydraulically-actuated, soft growing robot with a soft, tendon-driven notched continuum robot to overcome the challenges of steering for small-scale growing robots in endovascular procedures. The soft notched continuum robot successfully steers around the most difficult aortic arch type, and a 2.67 mm diameter growing robot—comparable in size to current catheters—deploys from the tip, pulling an aspiration catheter through extremely tortuous vessels. We present the design, manufacturing, and control of the notched continuum robot, growing robot, and proximal actuation subsystem. Overall, this robotic architecture facilitates active steering in proximal anatomy and navigation in tortuous distal vessels, with potential to reduce procedure times and expand access to care.

Keywords

Medical robotics; endovascular surgery; soft robotics; continuum robots; mechanical thrombectomy

I. Introduction

STROKE is one of the leading causes of death and disability in the US and worldwide [1]. The standard-of-care for ischemic stroke includes mechanical thrombectomy, which requires a trained neurointerventionalist to manually insert a series of catheters and guidewires into the femoral or radial artery and twist/turn them in order to steer through the arterial anatomy. Although the middle cerebral artery (MCA) is the most common artery involved in acute ischemic stroke due to large vessel occlusion [1], reaching the initial M1 segment can be challenging. Two of the most difficult areas to navigate are the aortic arch (particularly a type III) and the internal carotid artery (ICA), especially when it has high tortuosity [2]. Early time to treatment for ischemic stroke is significantly associated with positive patient outcomes [3]. However, due to the skills and training required to become a neurointerventionalist, there is geographic disparity of specialists, resulting in 33% of the US population not having access to endovascular therapy (EVT) within an hour [4]. A robotic system which can facilitate safe and efficient access to the M1 segment of the MCA could increase the number of EVT-capable centers through teleoperation and de-skilling the procedure, enhancing the availability and quality of stroke treatment.

A. Endovascular Continuum Robots

Several robotic systems have been proposed to help address the challenges of endovascular procedures. Notched nitinol tubes, for example, were shown to enable small-scale steering with the potential for self-steering through active compliance [5]. However, the steering has curvature limitations based on the amount of strain that nitinol can withstand. Guidewires with an articulating magnetic tip have been shown to navigate tortuous vessels [6], [7]. This technology requires external magnets whose footprint expands as the curvature requirement increases [7], potentially posing challenges when used with biplane fluoroscopy, which is used for live visualization during a mechanical thrombectomy. Soft robotic microcatheters that steer through fluidic pressure have been shown to achieve high curvatures in endovascular applications with the added benefit of being compliant [8], [9]. However, this actuation method requires high pressure and has been limited to a short bending segment which inhibits steering in free space (e.g., aortic arch).

Similarly, a few systems have been approved by the FDA for endovascular procedures (Magellan from Hansen Medical, Amigo from Catheter Precision, CorPath from Corindus, and Niobe from Stereotaxis) [2], [10], [11]. Despite the benefits of these systems, adoption has been limited due to cost and ease-of-use [10], along with limitations in the tortuosity of the path they can navigate. Because these robotic catheters are advanced via pushing from the base, they, like conventional handheld aspiration catheters, must balance stiffness—which risks endothelial damage or vascular spasm—and softness—which can lead to catheter buckling as friction increases [8], [12]. These inherent limitations in sliding friction and curvature are particularly relevant when navigating a tortuous path.

B. Growing Robots

In contrast to these push-based systems, soft growing robots navigate by extending from the tip, which allows for minimal interaction forces with the environment [13]. Growing robots consist of a compliant, thin-walled tube which has been inverted inside itself at one end. When pressurized, this inverted material everts from the tip, allowing for follow-the-leader navigation and for the compliant device to “find” paths of least resistance. Although previous work dating back decades has shown the value of eversion in surgical applications [14], [15], specifically vascular applications, reliable steering remains a major limitation [12].

Recent work has shown how growing robots can navigate by passively exploiting contact with the environment [16] or by using a prebend in the soft growing robot itself [17], [18]. Although this approach can enable navigation around the aortic arch, success depends heavily on the proper location of the prebend and can vary due to patient-specific anatomical variations. Another approach is to integrate an active steering mechanism into the soft growing robot body, typically using pneumatic artificial muscles [19], [20] or tendon-driven mechanisms [21]. However, these designs are difficult to scale down for medical applications, prompting the design of a tendon-driven, notched nitinol tube housed inside the soft growing robot [22]. Because the notched tube is not contained within the pressurized medium, it translates at twice the speed of the soft growing robot and requires a duty-cycling approach to align the tips. Furthermore, the curvature the soft growing robot can achieve is constrained by the strain limits of nitinol.

C. Contributions

The contributions of this work are as follows. (1) To overcome the challenges of steering for small-scale soft growing robots during mechanical thrombectomy procedures, we propose a new robot architecture that combines the distinct advantages of two serially-connected soft continuum robots. The tendon-actuated notched continuum robot has precise, active steering and delivers the hydraulically actuated soft growing robot, which is able to navigate through constrained, highly curved paths. The soft growing robot minimizes interaction forces with its surroundings by advancing via tip eversion and by pulling the aspiration catheter in tension, therefore eliminating the need for a guidewire and enabling a fully soft system. (2) To achieve this new robotic architecture, we present a new approach for 3D printing a soft tendon-driven notched continuum robot, involving the design of Eulerian paths which ensure a clear working channel through which the soft growing robot can evert. Additionally, we detail the manufacturing of a small-scale (2.67 mm diameter) soft growing robot and its integration with a watertight actuation system. (3) Finally, we present, to the best of our knowledge, the first soft growing robotic system to reach and aspirate within the middle cerebral artery (MCA). We demonstrate its ability to navigate the most challenging aortic arch (type III), traverse an extremely tortuous internal carotid artery (ICA) without blocking blood flow, and aspirate a mock blood clot (Fig. 1).

II. System Architecture and Workflow

In this section, we describe the overall system architecture by introducing the hybrid continuum robot and actuation subsystems. The hybrid continuum robot is the portion of the system that would extend inside the anatomy while the actuation subsystem would remain outside the patient (Fig. 2(a)).

A. Hybrid Continuum Robot

The hybrid continuum robot consists of a steerable notched continuum robot, along with a soft growing robot that is attached to its tip. The soft growing robot is initially inverted back inside the soft notched continuum robot, and an aspiration catheter is attached to the end of this growing component. The soft notched continuum robot consists of two coplanar, tendon-actuated, continuum segments and is used to steer around the aortic arch into the origin of the ICA (Step 1 in Fig. 1). The notched continuum robot then remains stationary while the soft growing robot deploys from the tip (Fig. 2(b)). The aspiration catheter is pulled (rather than pushed) forward in tension, enabling traversal of highly tortuous paths using a softer aspiration catheter and no guidewire.

After navigating from the ICA into the MCA, the aspiration catheter is exposed and able to access the clot. The user can then use current removal tools and processes, such as aspiration, where vacuum is applied to remove the blood clot. Because the soft growing robot everts, the length which can be aspirated in the MCA is twice the attachment distance (Fig. 2(b)) between the aspiration catheter and soft growing robot. To enable the soft growing robot to be pressurized for eversion, the entire hybrid continuum robot subsystem was made watertight using a sleeve.

B. Actuation Subsystem Architecture

The actuation subsystem contains all the components needed to control the notched continuum robot and soft growing robot. The main component is a watertight housing with two motor-driven capstans that actuate tendons to steer the notched continuum robot. This housing is mounted to a linear actuator to enable system insertion and can also be rolled by another motor to control the plane in which steering occurs. In order to control the soft growing robot's pressure, a syringe attached to a linear actuator is connected to the watertight housing. Proximal to the housing is a friction drive mechanism that controls the aspiration catheter's insertion. Because the soft growing robot is attached to the distal tip of the aspiration catheter, the friction drive mechanism controls the soft growing robot's length. The user interface of the system is a gamepad which enables the user to both steer in task space as well as actuate individual joints. Supplementary Video S1 shows the interface as well as the overall system architecture and workflow when deploying in a benchtop endovascular model.

III. Hybrid Continuum Robot Design and Manufacturing

In this section, we describe the manufacturing process for the notched continuum robot, as well as the design optimization that enables independence between the two notched continuum segments. We then describe the design and manufacturing of the soft growing robot and how it attaches to the notched continuum robot and aspiration catheter.

A. Notched Continuum Robot Manufacturing

The two segments of the notched continuum robot contain a series of notches that enable it to articulate when a tendon is pulled. Notched tubes have been used across a variety of applications and are typically made of nitinol using subtractive manufacturing techniques such as CNC milling [23] or femtosecond laser machining [24]. Additive manufacturing expands the design space of these notched tubes [25] and allows for quick design cycles. We select here to 3D print the notched continuum robot using a thermoplastic polyurethane (TPU) which is able to achieve extreme curvatures and, due to its soft nature, conform to the environment.

Due to the softness of the material (as compared to harder materials like PLA), FDM printing with TPU often results in stringing when moving in between extrusion points. This stringing can deposit unwanted material in critical areas (e.g., the clear working channel through which the soft growing robot must evert) and may also contribute to the print jamming. To mitigate these issues, we designed an Eulerian tool path [26], enabling our FDM printer (Bambu Lab X1C) to extrude continuously without lifting or jumping across the part. While previous work has leveraged Eulerian paths to ensure watertight seals across layers, our approach instead focuses on preserving a clear working channel. As a result, our layer design varies depending on the presence or absence of notches, prioritizing an unobstructed working channel for the soft growing robot to evert through. The designed SolidWorks part (Fig. 3(a)) included additional support and cutouts to enable a Eulerian path. As the print height increases, force from the FDM print head creates a greater moment on the part base. The designed support along the outside of the notched continuum robot countered this moment, and the designed support on the inside allowed for overhangs at each notch. The additional cutouts were based on which layers have a notch, resulting in two different Eulerian paths for each continuum segment. The difference between the inner and outer radii (r_i and r_o) of the tube was twice the printer nozzle diameter (0.4 mm) due to the designed Eulerian Path. This method enabled us to create a clear working channel without additional material or fraying (Fig. 3(c)). We also adjusted the Bambu slicer settings to print TPU with reduced stringing across the working channel, using the 0.12 mm fine presets, slower speeds (overhang 10 mm/s, bridge 5 mm/s), and reduced acceleration (1000 mm^2/s for the outer wall and default).

To determine the design requirements for steering around the type III aortic arch (described in Section VI-D), a circle was constructed concentric with the arch to estimate the required radius of curvature (less than 35 mm) and arc length (greater than 80 mm). The notch height h, notch depth g, uncut height c, and number of notches in the proximal notched continuum segment were adjusted to achieve the desired curvature. The notch parameters for the distal continuum segment were based on the optimization in Section III-B. After the notched continuum robot was printed, the additional support was removed manually, and Dyneema tendons (Dingbear 0.37 mm) were routed and terminated at the locations indicated in Fig. 3(a). The final designed and measured values are shown for both notch height and uncut height in Table I. Due to the unsupported overhang between the designed internal supports, the notch height was slightly lower than the designed part.

B. Distal Notched Continuum Segment Optimization

We performed a gradient-based design optimization to minimize the required actuation force for the distal segment of the notched continuum robot ($F_{\text{tendon},d}$). The ability to actuate the distal notched segment without largely affecting the proximal notched segment allows the robot to maintain purely kinematic control and use the Jacobian presented in Section V to enable steering in task space. In the following discussion and throughout the paper, the subscript (d) refers to parameters specific to the distal notched continuum segment and (p) for the proximal. The optimization problem was therefore:

$$\begin{aligned} \min_{g_d, h_d} \quad & F_{\text{tendon}, d}(g_d, h_d) \\ \text{subject to} \quad & \rho_{\min, d}(g_d, h_d) \leq 8.0 \text{ mm}, \\ & r_o \leq g_d \leq 5.0 \text{ mm}, \end{aligned} \tag{1}$$

where notch depth (g_d) and notch height (h_d) were the input variables. The first constraint required the distal segment of the notched continuum robot to have a minimum radius of curvature ($\rho_{\min, d}$) to successfully steer into the ICA after navigating around a type III aortic arch. Secondly, the notch depth (g_d) had to be larger than notched continuum robot outer radius for the notched section to have substantial bending compliance [23]. Additionally, the manufacturing capabilities, namely the amount of overhang, determined the upper bound for notch depth (described in Section III-A).

1) Objective Function Formulation: The notch depth (g_d) along with the inner and outer radii (r_i and r_o) of the tube determine the location of the distal segment's neutral axis:

$$\bar{y}_d(g_d) = \frac{4}{3}\left[\frac{r_o^3 \sin^3(\frac{1}{2}\phi_{o, d}(g_d)) - r_i^3 \sin^3(\frac{1}{2}\phi_{i, d}(g_d))}{r_o^2[\phi_{o, d}(g_d) - \sin \phi_{o, d}(g_d)] - r_i^2[\phi_{i, d}(g_d) - \sin \phi_{i, d}(g_d)]}\right] \tag{2}$$

where $\phi_{o, d}(g_d) = \arccos\left(\frac{g_d - r_o}{r_o}\right)$ and $\phi_{i, d}(g_d) = \arccos\left(\frac{g_d - r_o}{r_i}\right)$ [23], [24]. The highest actuation force occurs at the maximum articulation angle which was defined as $\theta_{\max, d}(g_d, h_d) = n_d \frac{h_d}{r_o + \bar{y}_d(g_d)}$. The strain ($\varepsilon$) in this configuration at location y_d was defined as:

$$\varepsilon(g_d, h_d, y_d) = \frac{\frac{1}{\rho_{\min, d}(g_d, h_d)}(y_d - \bar{y}_d(g_d))}{1 + \frac{\bar{y}_d(g_d)}{\rho_{\min, d}(g_d, h_d)}} \tag{3}$$

where $\rho_{\min, d}(g_d, h_d) \approx r_o + \frac{(n_d - 1)c_d}{\theta_{\max, d}(g_d, h_d)}$ was the minimum radius of curvature that can be attained and c_d was the uncut height between notches [23]. Assuming the TPU part had a constant Young's modulus E [27], the tendon force was

$$F_{\text{tendon}, d}(g_d, h_d) = \frac{E n_d h_d}{2\eta^{2 n_d} L_{t, d}(g_d)} \int_{A_{\text{cs}, d}} \varepsilon(g_d, h_d, y_d)^2 dA \tag{4}$$

where $A_{cs,d}$ is the cross-sectional area of the notched section (as y_d varies), $\eta < 1$ approximates the force lost due to friction, $L_{t,d}(g_d) = r_i - \frac{t_{dia}}{2} + \bar{y}_d(g_d)$ is the moment arm for the applied tendon force, and t_{dia} is the tendon diameter [23], [24]. To account for the worst case, the cross section was split into two sections: tension and compression which used r_o and r_i respectively for y_d.

2) Implementation, Parameter Sweeps, and Results: We used the SLSQP optimizer from the python-based modopt library [28] to perform the optimization and parameter sweeps. The SymPy library was used to find the objective gradients and constraint Jacobian. To account for uncertainty in friction, we conducted a parameter sweep across η (from 0.87-1.0) [29]. Additionally, the 3D printer's nozzle diameter determines the relationship between the inner and outer radii as shown in Section III-A, so we also did a parameter sweep for different nozzle diameters (0.2, 0.4, and 0.6). Across the parameter sweeps and even when varying the $\rho_{\min,d}$ constraint, maximizing g_d became most important with the optimized output being $g_d = 5.0$ mm and $h_d = 1.43$ mm. The manufacturing and optimization described above focused on a type III aortic arch. Future work will aim to extend the optimization across diverse anatomies to identify more generally applicable designs.

C. Soft Growing Robot Design and Manufacturing

The soft growing robot was manufactured by creating a thermoplastic polyurethane (TPU) tube by heat-bonding. A 20 μm thick TPU film (VLE-5001, American Polyfilm, Inc.) and a water-soluble tape (Aquasol) were first laser-cut into the desired dimensions. The length and the width of the water-soluble tape were equal to l_S and $2\pi r_s$, where l_S and r_S are the length and the radius of the soft growing robot, respectively. The water soluble tape with the fold line in the middle was attached to the TPU film, whose length was the same as l_S and the width was slightly wider than $2\pi r_s$ for an overlap. Then the assembly was folded into a flat tube with a lap joint (Fig. 4(a–b)), and the overlap was heat-bonded by heat pressing at 127°C for 60 seconds (Fig. 4(c)). The water soluble tape was dissolved in water (Fig. 4(d)).

The soft growing robot had a diameter of 2.67 mm (8 Fr) and a length of 445 mm. One end of the soft growing robot was attached using UV curing adhesive (AA3936, Loctite) to a 5 Fr aspiration catheter (SOFIA™, MicroVention, Inc.) commonly used in mechanical thrombectomy. The other end of the soft growing robot was attached to an SLA printed (Formlabs Inc.) tip mount which attached to the distal part of the notched continuum robot. Due to the notches, the notched continuum robot is not watertight, so we attached a sleeve made of a heat pressed TPU (152 μm thick, VLE-5001, American Polyfilm, Inc.) to the tip mount and base (Fig. 4(e)). The watertight sleeve was thick enough to withstand the maximum growth pressure of the soft growing robot while not noticeably affecting the kinematics of the notched tube.

IV. Actuation Subsystem Design

In this section, we detail the design of the steering and pressure subsystems. The steering subsystem contains all components which actuate the notched continuum robot in order to navigate the aortic arch, whereas the pressure subsystem is composed of the parts required to actuate the growing robot.

A. Steering Actuation

The notched continuum robot was actuated via Dyneema tendons wound around capstans that were housed in a two-part, waterproof enclosure. The capstans had threaded grooves to guide the tendons and maintain a consistent stroke length, and were driven by 12V DC-brushed geared motors (Pololu, 1000:1). Each capstan sat on two ball bearings, one at the base and one at the top (4 total), which were press fit into the watertight housing for smooth and constrained rotation. O-rings were used both between the base and the top of the enclosure and on the capstans to ensure pressure was maintained during rotation. The top of the housing contained an inlet lure lock fitting (for connection to the pressure subsystem), another lure lock fitting for venting which can be open or closed, and a hemostasis valve for aspiration catheter insertion. Both capstans and the watertight housing were 3D-printed (Bambu Lab X1C) using PETG filament. We adjusted the Bambu slicer settings for the housing base and top to withstand 85 kPa with minimal leakage (0.15 mm layer height, 8 wall loops, 8 top layers, 50% infill/wall overlap, 1.05 extrusion multiplier, and 255°C nozzle temperature). Additonally, we adjusted the 0.12 mm fine Bambu preset for the capstans to hold pressure and withstand the cable actuation tension (100% rectilinear infill density, 4 mm top shell thickness, and tree supports).

We controlled system roll with a DC Pololu motor mounted to a worm gear. System insertion was controlled by a linear actuator with a stepper motor (57H56H3004A2) commanded via a stepper motor driver (TB6600, EASON). We used micro-ROS [30] to connect an ESP32 microcontroller to ROS 2 (Humble) and command the motors used for steering the notched continuum robot. For the DC capstan motors, local motor control (PID) was run on the ESP32 utilizing the available encoder and commanding through a motor driver (L298N, Qunqi).

B. Pressure Subsystem

The pressure actuation system consisted of syringe (200cc) attached to a linear actuator (FA-OS-240-124, FIRGELLI Automations) which had a DC motor and encoder. The working fluid in the syringe and throughout the soft growing robot subsystem was 1% baby shampoo (Johnson's) which was the same as the fluid used in the benchtop endovascular model described in Section VI-D. The target pressure was set by a potentiometer (KY-040, JTAREA) which could also toggle whether pressure control was active or not.

A proportional controller in combination with a pressure sensor (ABPMANT100PG2A3, Honeywell) ensured the target pressure was maintained as the soft growing robot everts. A 12V DC-brushed geared motor (Pololu, 1000:1) commanded through a motor driver (L298N) rotates the wheel of the friction drive mechanism (purple in Fig. 5) to control the length of the soft growing robot after the measured pressure reaches above the target growth pressure (35 kPa in Section VI-D). All components in the pressure subsystem as well as the roll motor were run on a Teensy 4.1 microcontroller.

V. Modeling and Control

This section highlights the forward kinematic mapping from configuration to task space, and the inverse kinematic mapping from task space to actuator space. The forward kinematics is based on existing models [23] and additional considerations specific to our notched continuum robot. The inverse kinematics enabled the user to control the pose (position and orientation) of the tip of the robot in the steering plane.

A. Steering Forward Kinematics

The base frame {s} is defined as the location of the shaft attachment (Fig. 5) when the system insertion (q_{ins}) and system roll (q_{roll}) are zero. The translation along the z-axis by q_{ins} and shaft length (l_{shaft}) are represented by $T_{z,q_{\text{ins}}}$ and $T_{z,q_{\text{shaft}}}$ respectively. Likewise, the rotation about the z-axis by q_{roll} is $R_{z,q_{\text{roll}}}$. The transformation from the base frame {s} to the base of the proximal notched continuum segment $\{0_{pc}\}$ is

$$T_{s0_{pc}} = T_{z,q_{\text{ins}}} R_{z,q_{\text{roll}}} T_{z,q_{\text{shaft}}} R_{z,-90^{\circ}}. \tag{5}$$

Figure 6 shows frames $\{0_{pc}\}, \{1_p\}$, and $\{1_{pc}\}$ where (p) represents the proximal notched segment (d for the distal). The number corresponds to the notch number, and the (c) subscript is included if the the frame is above the uncut height (c).

For the notched continuum segments, piecewise constant curvature forward kinematics were used to map tendon actuation to curvature through a series of homogeneous transformations [23]. The distal segment of the notched continuum robot used the established neutral axis calculation shown in Eq. (2). The proximal notched segment had a different cross-sectional area due to the tendon routing channel (Fig. 6), so the updated equation for the location of its neutral axis was:

$$\bar{y}_p = \frac{\bar{y}_o A_o - \bar{y}_i A_i + \bar{y}_t A_t}{A_o - A_i + A_t} \tag{6}$$

where $\bar{y}_o$, A_o, $\bar{y}_i$, and A_i are the respective neutral axes and areas defined in [23], $A_t = A_1 - A_2 + A_3 - A_4 - A_5 + A_6$ is the additional cross-sectional area for tendon routing (see Fig. 6), and its neutral axis ($\bar{y}_t$) is given as:

$$\bar{y}_t = (\bar{y}_1 A_1 - \bar{y}_2 A_2 + \bar{y}_3 A_3 - \bar{y}_4 A_4 - \bar{y}_5 A_5 + \bar{y}_6 A_6)/A_t. \tag{7}$$

The areas and their respective neutral axes are defined in the Supplementary Information file. For both notched continuum segments, the transformation of each individual notch (j) is represented by $T_{j_c}^{j+1}$ and is dependent on the curvature (κ_j) and arc length (s_j) of the individual notch j:

$$\kappa_j \approx \frac{\Delta l}{h(r_i + \bar{y}) - \Delta l \bar{y}} \quad \text{and} \quad s_j = \frac{h}{1 + \bar{y}\kappa_j} \tag{8}$$

$$T_{j_c}^{j+1} = \begin{bmatrix} 1 & 0 & 0 & 0 \\ 0 & \cos(\kappa_j s_j) & -\sin(\kappa_j s_j) & (\cos(\kappa_j s_j) - 1)/\kappa_j \\ 0 & \sin(\kappa_j s_j) & \cos(\kappa_j s_j) & \sin(\kappa_j s_j)/\kappa_j \\ 0 & 0 & 0 & 1 \end{bmatrix} \tag{9}$$

where Δl represents tendon displacement per notch [23]. The remaining notched continuum robot parameters are defined in Table I with their respective values. The transformation from the base of proximal notched continuum segment $\{0_{pc}\}$ to its end $\{n_p\}$ is:

$$T_{0_{pc}n_p} = \left(\prod_{j=0}^{n_p - 1} T_{j_c}^{j+1} T_{z, c_p} \right) T_{z, -c_p} \tag{10}$$

where $n_p = 27$ is the number of notches [23]. The transformation between the notched continuum segments is $T_{n_p 0_{dc}} = T_{z, l_{\text{spacer}, p}} R_{z, 180^\circ}$ as the distal notched segment articulates in the opposite direction and there is a spacer of length $l_{\text{spacer}, p}$ for tendon termination. The transformation from the base of the distal notched segment $\{0_{dc}\}$ to the tip frame $\{\text{t}\}$ is:

$$T_{0_{dc}\text{t}} = \left(\prod_{j=0}^{n_d - 1} T_{j_c}^{j+1} T_{z, c_d} \right) T_{z, -c_d} T_{z, l_{\text{spacer}, d}} R_{z, -90^\circ}. \tag{11}$$

The series of transformations from the base frame $\{\text{s}\}$ to the tip coordinate frame $\{\text{t}\}$ is thus:

$$T_{\text{st}} = T_{\text{s}0_{pc}} T_{0_{pc}n_p} T_{n_p 0_{dc}} T_{0_{dc}\text{t}}. \tag{12}$$

B. Steering Inverse Kinematics

Controlling the notched continuum robot tip position in task space allows for more intuitive control for the user. Additionally, the angle of engagement between the soft growing robot and the environment as it everts largely affects the required growth pressure [31]. We therefore developed the following inverse kinematic mapping which allows the user to command tip position while maintaining orientation and command tip orientation while maintaining position. The user sends commands with a gamepad (Logitech F310) to control the x and z position of the {t} frame shown in Fig. 6. Similarly, the user can command rotation of the {t} frame about the y-axis to control the soft growing robot's deployment orientation. The steering plane (i.e. system roll, q_{roll}) is controlled separately from the inverse kinematics and is used to align with the top view, similar to the standard workflow that uses bi-plane fluoroscopy during a mechanical thrombectomy.

We used the Newton-Raphson method [32] to determine the joint-space trajectory for system insertion and tendon displacement of both the distal and proximal notched continuum segments. The Jacobian and spatial velocity for a continuum segment (the γ^{th} section) were defined in [33] as:

$$J_\gamma^s = \begin{bmatrix} s_e & \kappa_e \\ 0 & 0 \\ 0 & 0 \\ 0 & 0 \\ \frac{1-\cos(\kappa_e s_e)}{\kappa_e^2} & 0 \\ \frac{\kappa_e s_e - \sin(\kappa_e s_e)}{\kappa_e^2} & 1 \end{bmatrix} \quad \text{and} \quad V_\gamma^s = J_\gamma^s \begin{bmatrix} \dot{\kappa}_e \\ \dot{s}_e \end{bmatrix}. \tag{13}$$

We estimated the effective arc length (s_e) as the sum of the piecewise constant curvature notch sections and uncut sections between them. The effective curvature (κ_e) of each notched continuum segment was found through the relationship $\theta_e = n\theta_j$ and $\theta = s\kappa$ for both an individual notch (j) and the whole continuum segment (e).

$$s_e = n(s_j + c) - c \quad \text{and} \quad \kappa_e = \frac{n s_j \kappa_j}{s_e} \tag{14}$$

Figure 6 shows s_e and κ_e for the proximal notched continuum segment. We found both $\dot{s}_e$ and $\dot{\kappa}_e$ analytically with respect to tendon displacement Δl. The optimization in Section III-B proposed a way to minimize the effect of articulating the distal notched segment on the proximal notched segment, so we assume independent control over the two notched continuum segments. Applying the relevant adjoint transformations similar to [33], the Jacobian is:

$$J_{\text{robot}}^s = \left[J_0 \ \text{Ad}_{T_{s0_{pc}}} J_1 \ \text{Ad}_{T_{s0_{dc}}} J_2 \right] \tag{15}$$

where joint 0 is system insertion, joint 1 is the proximal notched continuum segment, and joint 2 is the distal. The effective arc length and curvature assumptions were sufficient as the numerical IK was able to converge while testing throughout the workspace and during the full system experiment. Supplementary Video S1 shows the teleoperation interface which allows users to control the robot in two modes: individual joint control and tip pose control in task space.

VI. Experiments and Results

We conducted experiments to verify (i) the accuracy of the forward kinematics model, (ii) the accuracy of independently controlling the two continuum joints, and (iii) the performance of the inverse kinematics. We performed all experiments in a single plane using an electromagnetic (EM) sensor and field generator (Northern Digital Inc.) for tracking, and we used only the notched continuum robot, without the soft growing robot and watertight sleeve (which are thin and have negligible affect on steering). The final experiment validated the system architecture by deploying the system in a benchtop anatomical model and aspirating a mock clot.

A. Forward Kinematics

To characterize the accuracy of the kinematic model, we attached the EM sensor at the midpoint between coordinate frames $\{n_p\}$ and $\{0_{dc}\}$ (Fig. 6) for the proximal notched continuum segment and at the midpoint between coordinate frames $\{n_d\}$ and $\{t\}$ for the distal notched segment. When evaluating the distal notched segment, we secured its base to isolate that section. We actuated the tendon in 1 mm increments from zero to maximum articulation (Pass 1) and from maximum articulation back to its home position (Pass 2) as shown in Fig. 7. We computed the normalized root mean square error (NRMSE) between the model tip position to the measured tip position similar to [25]:

$$err = \frac{1}{L}\sqrt{\frac{\sum_{i=1}^{N}\left(\|P_i - \hat{P}_i\|\right)^2}{N}} \tag{16}$$

where P_i was the recorded position, $\hat{P}_i$ was the position predicted by the model, N was the number of points collected, and L was the length of the articulated section (from the base of the notched continuum segment to the EM sensor). We used the parameter values defined in Table I, specifically the measured values for cut depth (g) and height (h). To demonstrate repeatability, we tested each notched continuum segment three times with a representative trial shown in Fig. 7.

Across all trials the NRMSE for the proximal notched segment was 9.9±1.2% the continuum length. Consistent with other notched tube papers [23], the error can likely be attributed to two of the primary model assumptions: (1) the notched section undergoes simple bending as a beam and (2) the uncut sections behave as rigid bodies. Oliver-Butler et al. [25] showed these assumptions were less likely to be true when the uncut height was greater than or equal to the cut height $c \geq h$, which is true for the proximal notched segment. Additionally, the deformation of the uncut sections is likely exacerbated by the softness of TPU compared to nitinol. Lastly, Eq. (10) and Eq. (11) assume constant curvature across all individual notches, which is not necessarily true.

The overall NRMSE for the distal notched segment was 17.6±0.7%, which was larger than that of the proximal notched segment likely due to hysteresis. Figure 7(b) shows how Pass 2 (NRMSE = 23.0±0.7%) was not able to return to straight and thus had a higher error than Pass 1 (NRMSE = 9.3±1.1%). Because we optimized the design of the distal segment of the notched continuum robot with the goal of reducing the required actuation force, the restoring force was too small to overcome the friction along the tendon path to fully straighten. Additionally, because both notched continuum segments achieved such high curvature, there was some plastic deformation, which can be seen in the starting offset between Pass 1 and the model home (straight) position.

B. Joint Independence

To evaluate the joint independence achieved through the optimization in Section III-B, we conducted the following experiment, which demonstrated that the distal notched continuum segment had minimal impact on the proximal notched continuum segment when articulating. We attached an EM sensor at the end of the distal notched segment and another at the end of the proximal notched segment. Starting with the notched continuum robot in the home position, we commanded the distal notched segment to full articulation and then back to zero (purple in Fig. 8), while measuring the movement in the proximal notched continuum segment (red in Fig. 8). We then commanded the proximal notched continuum segment to another articulation and repeated the experiment for a total of seven configurations throughout the workspace.

We calculated the NRMSE using Eq. (16) where $\hat{P}_i$ was the initial position of the proximal EM sensor (Fig. 8) for that configuration, P_i was the recorded position with the maximum distance, N was the number of articulations, and L was the length from the base of the proximal notched continuum segment to the EM sensor. The NRMSE was 5.2% (5.4 mm), which was nearly half the NRMSE for the proximal notched segment alone (Section VI-A), and was deemed sufficiently small enough to allow for independent actuation of the two notched continuum segments. This joint independence experiment, along with the inverse kinematics testing, validated the optimization performed in Section III-B for enabling independent joint actuation.

C. Inverse Kinematics

The following two experiments validated the inverse kinematic mapping and evaluated the accuracy of independently controlling the position and orientation of the tip frame {t}. In the first experiment, we commanded the tip position to change, while maintaining orientation. In the second experiment, we commanded a change in orientation, while maintaining position. For both tests, we attached an EM sensor to the end of the notched continuum robot at the midpoint between the $\{n_d\}$ and {t} coordinate frames.

The first experiment showed that the {t} frame was able to maintain an upward orientation while commanding a Lissajous pattern (Fig. 9) similar to the one used in [34]. We chose a vertical orientation for the tip as it reflects deployment of the soft growing robot up the ICA. The tip frame {t} changed x and z position over 40 mm each while having a maximum rotation deviation from the start orientation of 11.4 degrees (mean = 5.8±3.4 degrees). Soft growing robots can deploy along obstacles, even at near perpendicular angles [16], so a maximum deviation of 11.4 degrees was more than acceptable.

For the second inverse kinematics experiment we commanded change in tip orientation while maintaining position. For tip position I in Fig. 10, we articulated the notched continuum segments so the tip frame was near the edge of the workspace and still allowed for orientation control. The tip frame {t} maintained position while changing orientation until its z-axis was near vertical, enabling deployment of the soft growing robot up the ICA. The commanded angle was broken into 5 equal angles and then the notched continuum robot was commanded back to its original orientation, for a total of 10 poses. A conceptual overlay of the initial and max rotation configurations of the notched continuum robot in Fig. 10 show how the curvatures and system insertion update to change deployment orientation while maintaining position. At each pose, we calculated the error in x and z by finding the offset from the starting position. We repeated this process for the three trials to determine the mean and standard deviation for each pose. We conducted a similar experiment for two other tip positions (II in orange and III in brown in Fig. 10) to show the capabilities at different locations in the workspace. Because these positions resulted in starting configurations where the {t} z-axis orientation was nearly vertical, the maximum commanded orientation came from rotating {t} clockwise about the y-axis until nearing the joint limit of one of the notched continuum segments.

Tip position I (green in Fig. 10) had the largest commanded rotation, resulting in a maximum z-direction error of 11.0 mm (7.2% of the articulated length). This error was primarily due to hysteresis in the distal continuum segment, which prevented the tip from fully returning to its original position (Pass 2 in Section VI-A). As expected, Positions II and III exhibited significantly smaller z-direction errors. However, Tip Position III showed the largest x-direction error, likely caused by plastic deformation of both continuum segments, as described in Section VI-A. Both these errors occur when the tendons are slack and are therefore acceptable even during soft robot-environment contact. While the diameter at the origin of the ICA (7.59±1.00 mm) [35] is slightly smaller than the maximum positioning error, the teleoperated system enables real-time user adjustments, allowing successful steering into the ICA origin. To improve accuracy, future work could reduce positioning error by making the notched continuum segments antagonistic or by incorporating a design constraint on acceptable strain (Eq. (3)) for each notch.

D. Full System Deployment

1) Endovascular Benchtop Model: We used a silicon vasculature model (Trandomed), similar to those used for clinical training and testing other endovascular devices, to evaluate the full system architecture. The 3D benchtop model (Fig. 11(a)) was representative of a challenging case, including a type III aortic arch and a tortuous ICA comprised of two 360-degree loops with 7.3 mm radius of curvature, two 180-degree bends (6.2 and 4.2 mm radii of curvature), and a 4.6 mm siphon bend before MCA (Fig. 11(g–i)). Throughout the 360-degree loops and 180-degree bends, the tortuous ICA model had an inner diameter tapering from 5.4 mm to 4.1 mm, closely reflecting the mean patient anatomy [36]. The 2.67 mm diameter growing robot is similar in size to existing 6 Fr shuttles (2.6

mm OD) used during mechanical thrombectomy [37] and was able to pull the 5F aspiration catheter through the ICA without occluding blood flow. The fluid in the model was water with 1% baby shampoo (Johnson's), which is commonly used in endovascular models as it more closely simulates the friction properties of blood. We used the same fluid to pressurize the soft growing robot. For the mock blood clot, we used putty (JA-RU, Flarp!), similar to recent work [38].

2) System Deployment: Supplementary Video S1 shows the full system deployment and successful aspiration of the mock blood clot. The user view of the anatomical model (Fig. 11(b)) simulated the operator view currently used in mechanical thrombectomy (enabled by bi-plane fluoroscopy) and provided a visualization of the steering subsystem. The user interface allowed the operator to steer the notched continuum robot tip in task space (mapping shown in Fig. 11(c)), as well as actuate joints individually.

We first slacked the tendons in the soft notched continuum robot, allowing it to insert and passively conform to the aortic arch (Fig. 11(d)). We then tensioned the tendon for the proximal notched continuum segment until movement was seen, and the same was done for the distal notched segment. We then steered the tip into the base of the tortuous ICA, with the orientation adjusted to deploy the soft growing robot along the vessel wall rather than into it (Fig. 11(e)).

To deploy the soft growing robot, we increased the pressure (35-40 kPa) and commanded the friction drive mechanism to release the aspiration catheter, allowing the soft growing robot to continually evert around the tortuous ICA and pull the aspiration catheter in tension (Fig. 11(g–h)). The aspiration catheter reached the MCA, became exposed, and then came in contact with the mock blood clot (Fig. 11(h–i)). We attached a vacuum line to the proximal part of the aspiration catheter and successfully removed the mock blood clot (Fig. 11(j)).

The soft growing robot's pressure was decreased and the aspiration catheter was retracted. As seen in the Supplementary Video S1, the growing robot initially inverted at the distal end where the diameter was constrained, and then scrunched during retraction in areas where it was unconstrained (at the origin of the ICA). After retracting the aspiration catheter, the soft notched continuum robot was released from tension and retracted. This work was, to the best of our knowledge, the first time a soft growing robot was able to reach the MCA of a benchtop model and aspirate a mock blood clot. The entire process was completed in less than 10 minutes.

The system pressure was increased to deploy the soft growing robot only after steering into the origin of the ICA. This change in stiffness had a negligible effect on the notched continuum robot configuration when steering into the type III aortic arch, and was therefore not included in the modeling. During deployment, the SOFIA aspiration catheter increased in stiffness as the soft growing robot was deployed (the gray is less stiff than the green portion in Supplementary Video S1), so the force exerted on the notched continuum robot changed throughout deployment. Towards the end, the notched continuum robot tip position changed due to the force exerted on it, but it was able to maintain an orientation and continue successfully deploying the soft growing robot. We used a SOFIA aspiration catheter due to is soft distal end and availability. Future systems could utilize other aspiration catheters with similar stiffness (e.g., Penumbra Red) or, given the growing robot's ability to pull the catheter in tension, could develop a fully soft catheter that exerts even less force on the environment. Future work will also concentrate on minimizing notched continuum robot movement during the deployment of the aspiration catheter and enhancing the design by decreasing its diameter. Finally, similar to existing robotic tools (da Vinci stapler, vessel sealer, etc.), we envision that the hybrid continuum robot and watertight housing would be sterilized for one-time use, while the actuation subsystem would include a disposable interface.

VII. Conclusion

In this work, we introduced a novel robotic architecture composed of two serially-connected soft continuum robots: a notched continuum robot for steering and a growing robot capable of navigating constrained, highly tortuous paths. We detailed the system's design, fabrication, and control, demonstrating its capability to traverse a type III aortic arch and reach the ICA and M1 segment of the MCA, which are the regions most frequently targeted during mechanical thrombectomy procedures [39]. The architecture has potential to empower trained neurointerventionalists to perform mechanical thrombectomy more quickly, and to increase access to stroke care through teleoperation and deskilling the procedure. Future enhancements, such as embedding actuators within the skin of the growing robot, could extend steering capabilities to reach more distal occlusions, including those in the M2 segment.

To better understand the system's performance under more realistic physiological conditions, such as pulsatile motion, blood flow, and vessels with frictional properties more similar to human vessels, we plan to assess the system in vivo through an acute animal study. As part of this evaluation, we will mix a contrast agent into the pressurization fluid to visualize the growing robot [18] and notched continuum robot under fluoroscopy, as well as integrating a dedicated internal channel that delivers contrast agents to the distal tip to enable vascular blood flow assessment before and after the thrombectomy. We will perform histological evaluations to compare the tissue interactions of our eversion-based design to conventional push-based catheters and guidewires. Finally, we plan to thoroughly investigate the generalizability of our design across patient anatomies, and will explore using computed tomography angiography (CTA), which is typically performed before a mechanical thrombectomy, for dimensional adjustments if needed.

Supplementary Material

Refer to Web version on PubMed Central for supplementary material.

Acknowledgment

This work was supported in part by the National Institute of Health under R01 EB032417 and by the National Science Foundation under Grant 1944816. AM was also supported in part by the Powell Fellowship (Charles Lee Powell Foundation). The authors of this manuscript have patents on soft growing robot technologies. EH is a board member of Vine Medical, Inc., which holds a license to some of these patents.

References

[1]. Nogles TE and Galuska MA, "Middle cerebral artery stroke," in StatPearls [Internet]. StatPearls Publishing, 2023.

[2]. Ghamraoui AK and Ricotta JJ, "Current and future perspectives in robotic endovascular surgery," Current Surgery Reports, vol. 6, pp. 1–7, 2018.

[3]. Asdaghi N, Wang K, Gardener H, Jameson A, Rose DZ, Alkhachroum A, Gutierrez CM, Ying H, Mueller-Kronast N, Sur NB et al. , "Impact of time to treatment on endovascular thrombectomy outcomes in the early versus late treatment time windows," Stroke, vol. 54, no. 3, pp. 733–742, 2023. [PubMed: 36848428]

[4]. Sarraj A, Farrell CM, Reishus K, Sharrief AZ, McCullough L, and Savitz SI, "Endovascular thrombectomy access in the united states: the current status and an optimization model," Stroke, vol. 49, no. Suppl_1, pp. A92–A92, 2018.

[5]. Abah C, Lawson JP, Chitale R, and Simaan N, "Self-steering catheters for neuroendovascular interventions," IEEE Transactions on Medical Robotics and Bionics, 2024.

[6]. Kim Y, Genevriere E, Harker P, Choe J, Balicki M, Regenhardt RW, Vranic JE, Dmytriw AA, Patel AB, and Zhao X, "Telerobotic neurovascular interventions with magnetic manipulation," Science Robotics, vol. 7, no. 65, p. eabg9907, 2022. [PubMed: 35417201]

[7]. Dreyfus R, Boehler Q, Lyttle S, Gruber P, Lussi J, Chautems C, Gervasoni S, Berberat J, Seibold D, Ochsenbein-Kölble N et al. , "Dexterous helical magnetic robot for improved endovascular access," Science Robotics, vol. 9, no. 87, p. eadh0298, 2024. [PubMed: 38354258]

[8]. Gopesh T, Wen JH, Santiago-Dieppa D, Yan B, Pannell JS, Khalessi A, Norbash A, and Friend J, "Soft robotic steerable microcatheter for the endovascular treatment of cerebral disorders," Science robotics, vol. 6, no. 57, p. eabf0601, 2021. [PubMed: 34408094]

[9]. Felix BM, Young OM, Andreou JT, Portwood N, Barvenik KJ, Barnes N, Weiss CR, Bailey CR, Gandhi D, Janowski M et al., "An approach for 3d microprinting soft robotic surgical tools at 1.5 french length scales for endovascular interventions," in 2024 IEEE 7th International Conference on Soft Robotics (RoboSoft). IEEE, 2024, pp. 386–391.

[10]. Shaikh ZA, Eilenberg MF, and Cohen TJ, "The amigo™ remote catheter system: from concept to bedside," The Journal of innovations in cardiac rhythm management, vol. 8, no. 8, p. 2795, 2017. [PubMed: 32494463]

[11]. Carpi F and Pappone C, "Stereotaxis niobe® magnetic navigation system for endocardial catheter ablation and gastrointestinal capsule endoscopy," Expert review of medical devices, vol. 6, no. 5, pp. 487–498, 2009. [PubMed: 19751121]

[12]. Goldstein S, Jones R, Sipe J, Doppman J, and Boretos J, "A miniature toposcopic catheter suitable for small diameter tortuous blood vessels," 1980.

[13]. Hawkes EW, Blumenschein LH, Greer JD, and Okamura AM, "A soft robot that navigates its environment through growth," Science Robotics, vol. 2, no. 8, p. eaan3028, 2017. [PubMed: 33157883]

[14]. Zeimer H and Simkin A, "Toposcopy. frictionless method of entering body cavities and tracts," New York state journal of medicine, vol. 66, no. 14, pp. 1925–1930, 1966. [PubMed: 5220277]

[15]. Shook D, Doppman J, Cattau E Jr, and Goldstein S, "Everting (toposcopic) catheter for broad clinical application," 1986.

[16]. Greer JD, Blumenschein LH, Alterovitz R, Hawkes EW, and Okamura AM, "Robust navigation of a soft growing robot by exploiting contact with the environment," The International Journal of Robotics Research, vol. 39, no. 14, pp. 1724–1738, 2020.

[17]. Slade P, Gruebele A, Hammond Z, Raitor M, Okamura AM, and Hawkes EW, "Design of a soft catheter for low-force and constrained surgery," in 2017 IEEE/RSJ International Conference on Intelligent Robots and Systems (IROS). IEEE, 2017, pp. 174–180.

[18]. Li M, Obregon R, Heit JJ, Norbash A, Hawkes EW, and Morimoto TK, "Vine catheter for endovascular surgery," IEEE Transactions on Medical Robotics and Bionics, vol. 3, no. 2, pp. 384–391, 2021.

[19]. Coad MM, Blumenschein LH, Cutler S, Zepeda JAR, Naclerio ND, El-Hussieny H, Mehmood U, Ryu J-H, Hawkes EW, and Okamura AM, "Vine robots," IEEE Robotics & Automation Magazine, vol. 27, no. 3, pp. 120–132, 2019.

[20]. Kübler AM, Rivera SU, Raphael FB, Förster J, Siegwart R, and Okamura AM, "A multi-segment, soft growing robot with selective steering," in 2023 IEEE International Conference on Soft Robotics (RoboSoft). IEEE, 2023, pp. 1–7.

[21]. Blumenschein LH, Koehler M, Usevitch NS, Hawkes EW, Rucker DC, and Okamura AM, "Geometric solutions for general actuator routing on inflated-beam soft growing robots," IEEE Transactions on Robotics, vol. 38, no. 3, pp. 1820–1840, 2021.

[22]. Berthet-Rayne P, Sadati SH, Petrou G, Patel N, Giannarou S, Leff DR, and Bergeles C, "Mammobot: A miniature steerable soft growing robot for early breast cancer detection," IEEE Robotics and Automation Letters, vol. 6, no. 3, pp. 5056–5063, 2021.

[23]. York PA, Swaney PJ, Gilbert HB, and Webster RJ, "A wrist for needle-sized surgical robots," in 2015 IEEE International Conference on Robotics and Automation (ICRA). IEEE, 2015, pp. 1776–1781.

[24]. Chitalia Y, Jeong S, Yamamoto KK, Chern JJ, and Desai JP, "Modeling and control of a 2-dof meso-scale continuum robotic tool for pediatric neurosurgery," IEEE Transactions on Robotics, vol. 37, no. 2, pp. 520–531, 2020.

[25]. Oliver-Butler K, Childs JA, Daniel A, and Rucker DC, "Concentric push–pull robots: Planar modeling and design," IEEE Transactions on Robotics, vol. 38, no. 2, pp. 1186–1200, 2021.

[26]. Zhai Y, De Boer A, Yan J, Shih B, Faber M, Speros J, Gupta R, and Tolley MT, "Desktop fabrication of monolithic soft robotic devices with embedded fluidic control circuits," Science Robotics, vol. 8, no. 79, p. eadg3792, 2023. [PubMed: 37343076]

[27]. Filament B, "Tpu 95a," 2022.

[28]. Joshy AJ and Hwang JT, "modopt: A modular development environment and library for optimization algorithms," arXiv preprint arXiv:2410.12942, 2024.

[29]. Lin J-T, Mangan A, and Morimoto TK, "Hcr: Haptic continuum robot for multi-modal cutaneous feedback," IEEE Robotics and Automation Letters, 2025.

[30]. Belsare K, Rodriguez AC, Sánchez PG, Hierro J, Kołcon T, Lange R, Lütkebohle I, Malki A, Losa JM, Melendez F et al. , "Micro-ros," in Robot Operating System (ROS) The Complete Reference (Volume 7). Springer, 2023, pp. 3–55.

[31]. Haggerty DA, Naclerio ND, and Hawkes EW, "Characterizing environmental interactions for soft growing robots," in 2019 IEEE/RSJ International Conference on Intelligent Robots and Systems (IROS). IEEE, 2019, pp. 3335–3342.

[32]. Lynch K, Modern Robotics. Cambridge University Press, 2017.

[33]. Webster III RJ and Jones BA, "Design and kinematic modeling of constant curvature continuum robots: A review," The International Journal of Robotics Research, vol. 29, no. 13, pp. 1661–1683, 2010.

[34]. Chikhaoui MT, Granna J, Starke J, and Burgner-Kahrs J, "Toward motion coordination control and design optimization for dual-arm concentric tube continuum robots," IEEE Robotics and Automation Letters, vol. 3, no. 3, pp. 1793–1800, 2018.

[35]. Baz RA, Scheau C, Niscoveanu C, and Bordei P, "Morphometry of the entire internal carotid artery on ct angiography," Medicina, vol. 57, no. 8, p. 832, 2021. [PubMed: 34441039]

[36]. Krejza J, Arkuszewski M, Kasner SE, Weigele J, Ustymowicz A, Hurst RW, Cucchiara BL, and Messe SR, "Carotid artery diameter in men and women and the relation to body and neck size," Stroke, vol. 37, no. 4, pp. 1103–1105, 2006. [PubMed: 16497983]

[37]. Medical C, "Flexor® shuttle® guiding sheath," 2025, accessed: 2025-02-05. [Online]. Available: https://www.cookmedical.com/products/di_ksawsh_webds/

[38]. Lawson J, Veliky M, Abah CP, Dietrich MS, Chitale R, and Simaan N, "Endovascular detection of catheter-thrombus contact by vacuum excitation," IEEE Transactions on Biomedical Engineering, 2024.

[39]. Bhogal P, Bücke P, AlMatter M, Ganslandt O, Bäzner H, Henkes H, and Aguilar Pérez M, "A comparison of mechanical thrombectomy in the m1 and m2 segments of the middle cerebral

artery: a review of 585 consecutive patients," Interventional neurology, vol. 6, no. 3-4, pp. 191–198, 2017. [PubMed: 29118796]

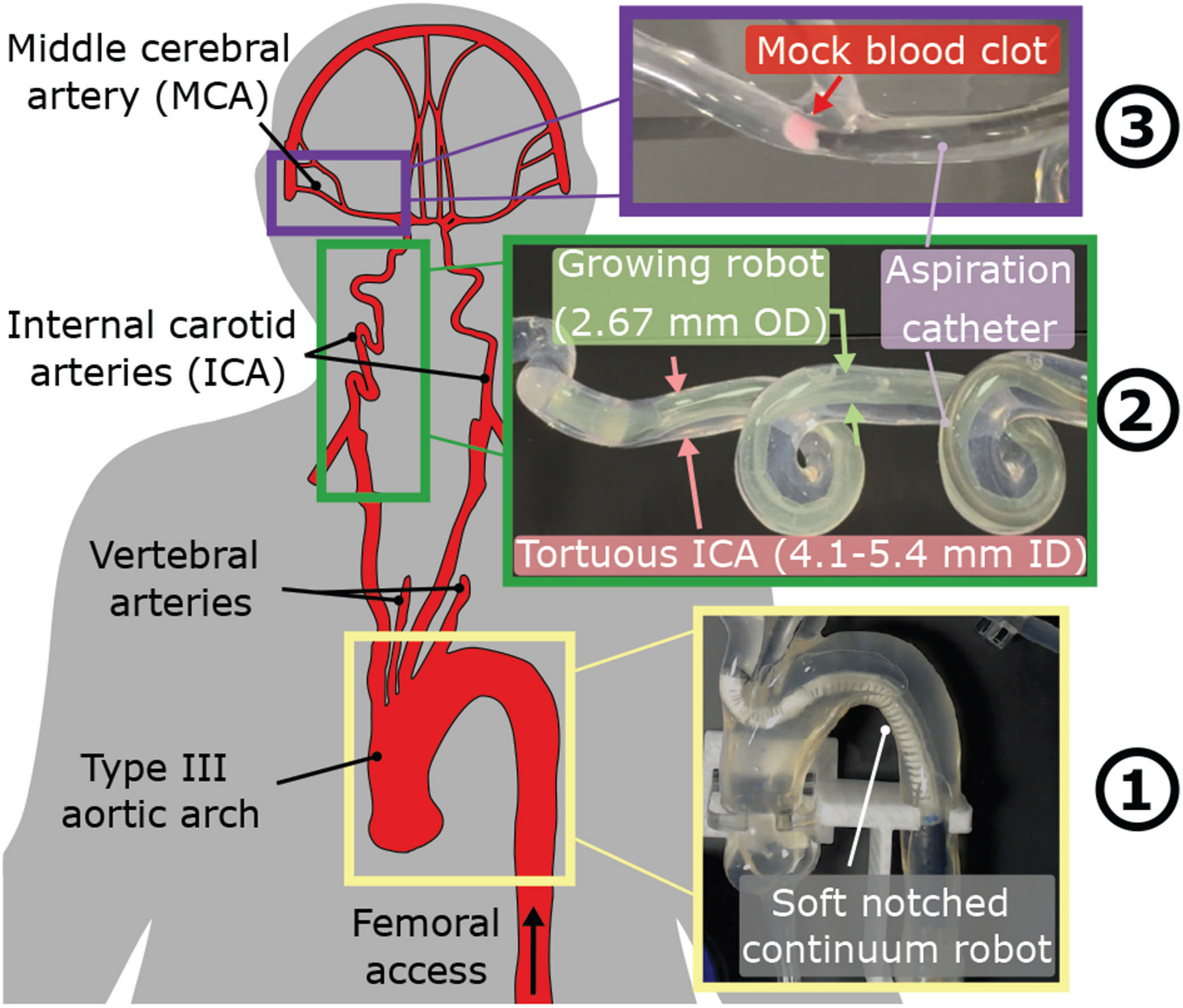

Fig. 1.

The system successfully (1) navigated a type III aortic arch with the soft notched continuum robot, (2) traversed a tortuous ICA with a soft growing robot (false-colored with green for better visibility), and (3) gained aspiration access for clot removal in the MCA. The system demonstrated the ability to perform the most demanding aspects of mechanical thrombectomy in a benchtop model representing highly challenging anatomy (type III aortic arch and extremely tortuous ICA).

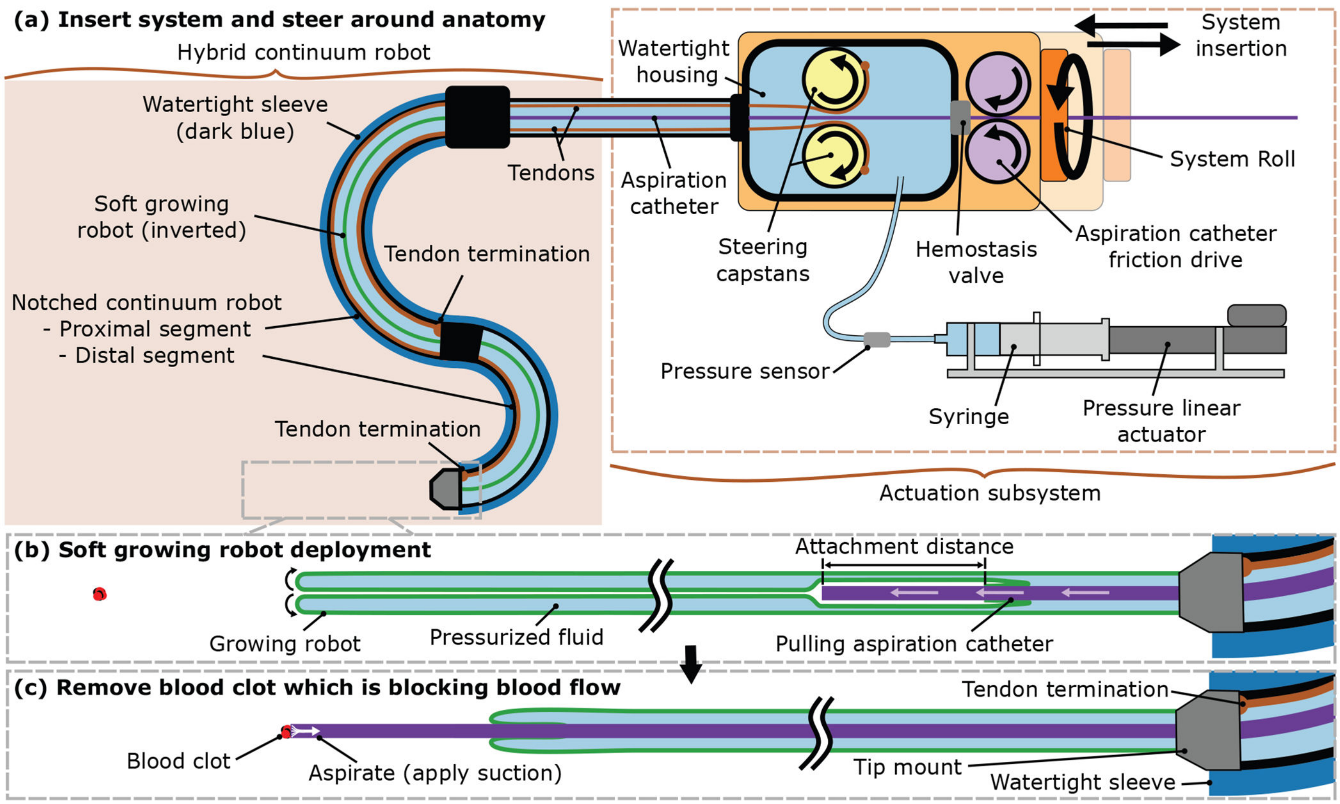

Fig. 2.

The system is composed of a hybrid continuum robot (inside the anatomy) and an actuation subsystem. The notched continuum robot has two segments which are driven by tendons attached to capstans (yellow) located in a watertight housing. The housing is mounted on a linear actuator for system insertion and a separate motor controls system roll. After (a) steering the hybrid continuum robot around the aortic arch, a soft growing robot (b) is deployed from the tip. The soft growing robot (green) is pressurized by fluid (light blue) and pulls the aspiration catheter (purple) forward. The soft growing robot is attached to the tip mount on one side and the aspiration catheter on the other. The attachment distance between the end of the growing robot and aspiration catheter enables access to the clot in the M1 segment of the MCA. Supplementary Video S1 shows the architecture, teleoperation, and full system deployment in a benchtop anatomical model.

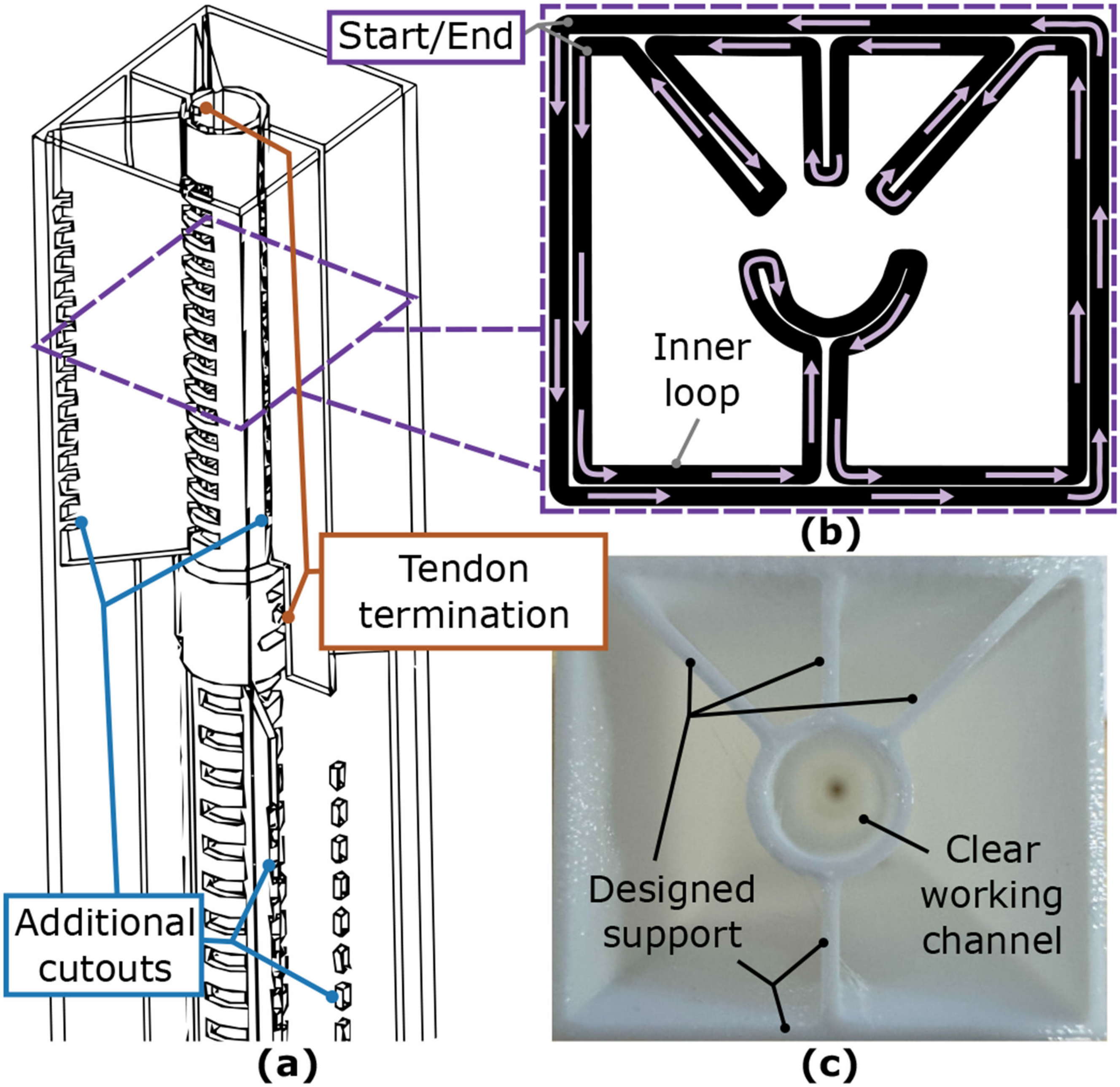

Fig. 3.

(a) The designed SolidWorks part with tendon terminations, external supports, and additional cutouts in order to form (b) a Eulerian path, allowing for (c) a clear working channel for the soft growing robot to pass through.

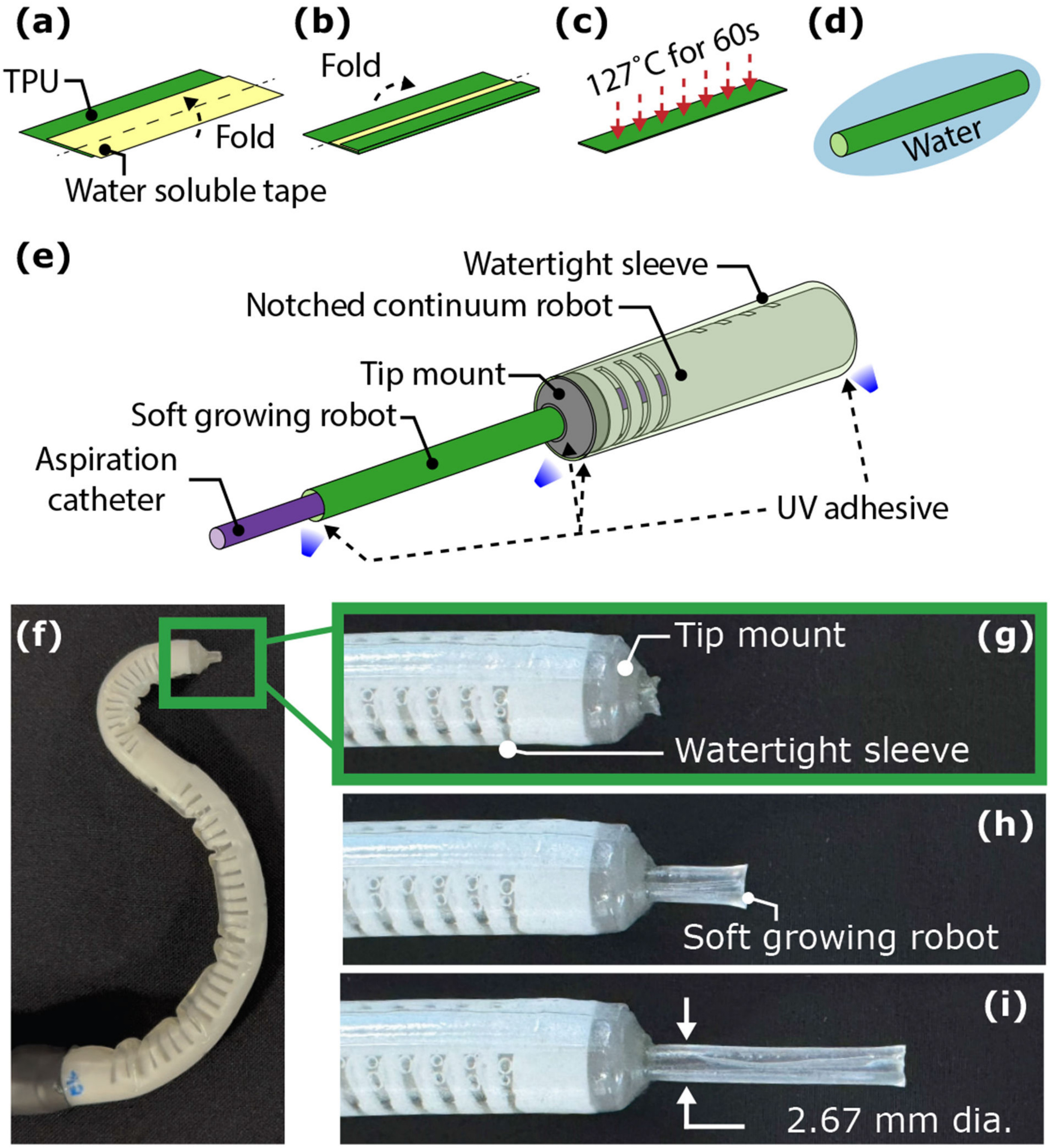

Fig. 4.

(a-d) The soft growing robot is made by heat pressing TPU and then dissolving the water soluble tape. The watertight sleeve is made through the same manufacturing process and (e) attaches to the notched continuum robot with UV cure adhesive. One end of the soft growing robot attaches to the tip mount and the other to the aspiration catheter. (f) An image of the fully assembled hybrid continuum robot in an articulated state. (g-i) show deployment of the soft growing robot after pressurizing and commanding the friction drive mechanism.

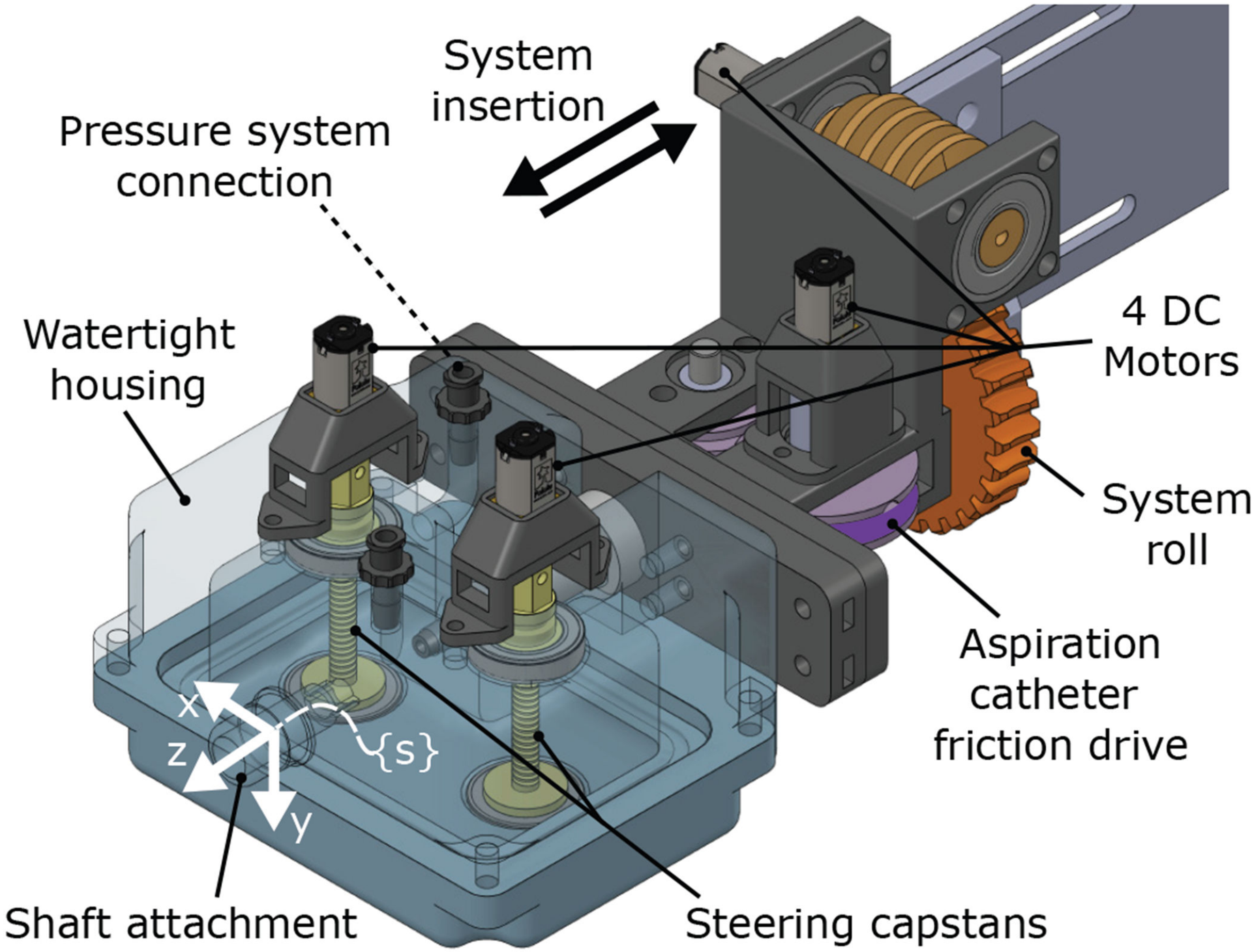

Fig. 5.

The actuation subsystem is comprised of a watertight housing (blue) which can withstand over 85 kPa and contains two steering capstans (yellow) attached to DC motors for driving the two notched continuum segments. The system roll (orange) is controlled by a DC motor connected to a worm gear whereas system insertion is actuated by a stepper motor (not shown). The aspiration catheter insertion and thus soft growing robot length are controlled by friction drive wheels (purple) attached to a DC motor. The design of this system allows for watertight steering of the soft notched continuum robot and deployment of the growing robot.

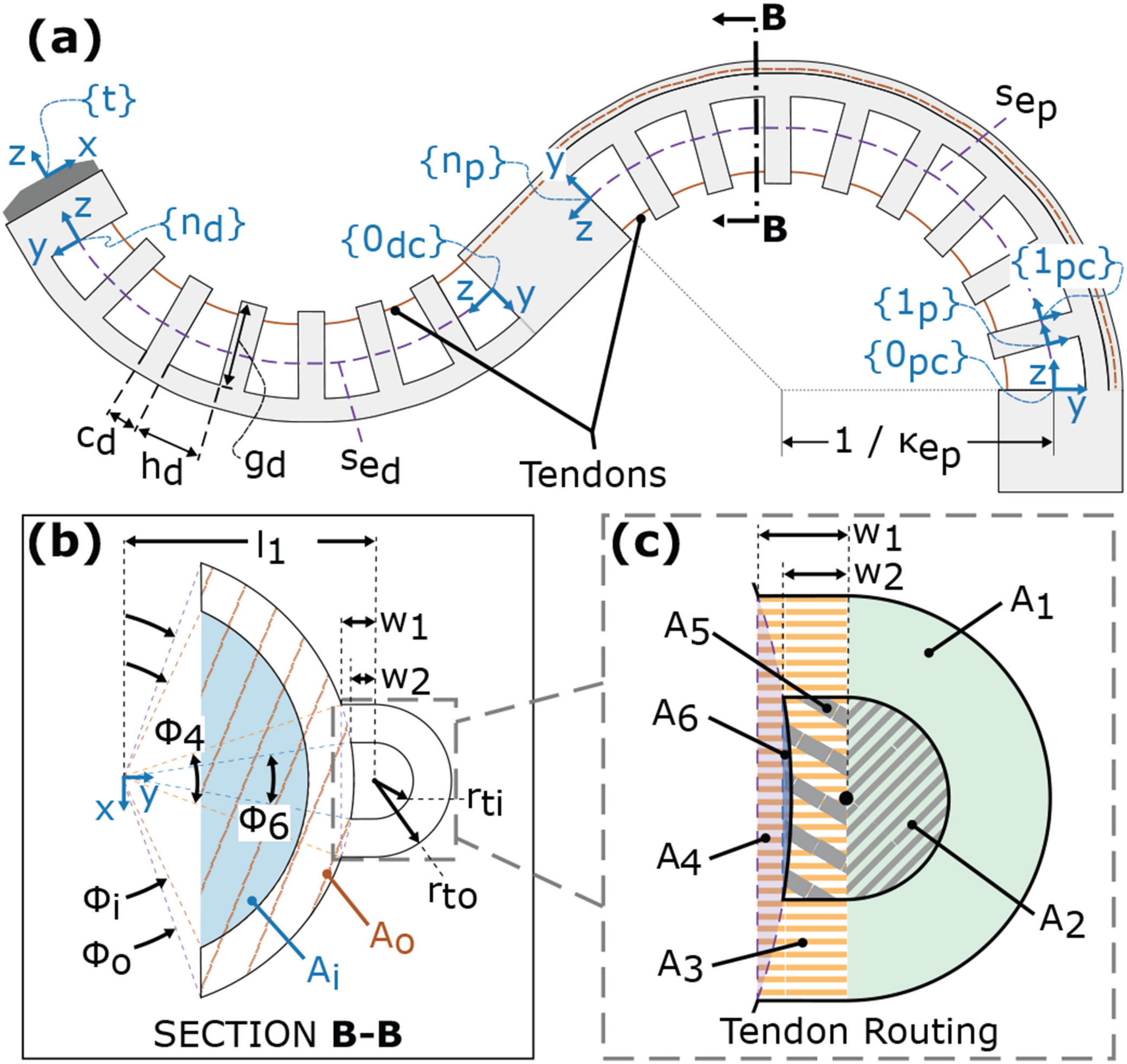

Fig. 6.

(a) The notched continuum robot design parameters including notch height (h_d), notch depth (g_d), and uncut height (c_d) are shown for the distal notched segment. (b) The cross-sectional area of the proximal notched segment includes a tendon routing channel of which (c) the geometry determines the updated neutral axis location. The coordinate frames are a result of homogeneous transformations along the notched continuum robot.

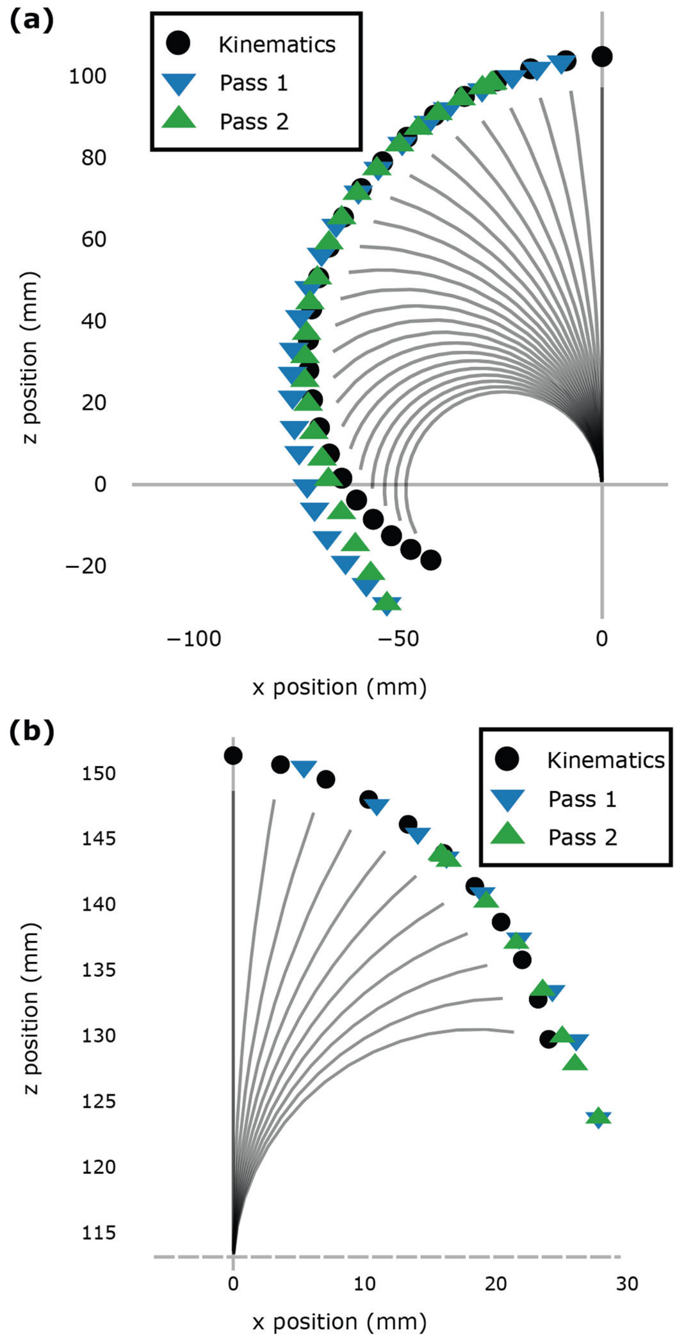

Fig. 7.

Experimental results compared to the kinematic model for (a) the proximal notched continuum segment and (b) the distal notched continuum segment. Each respective notched continuum segment was commanded from its zero position to maximum articulation (Pass 1) and then from maximum articulation back to zero (Pass 2). Note: only one of three trials is shown above for test method clarity, and the proximal notched continuum segment has a larger scale. Both segments tracked well to the kinematic model.

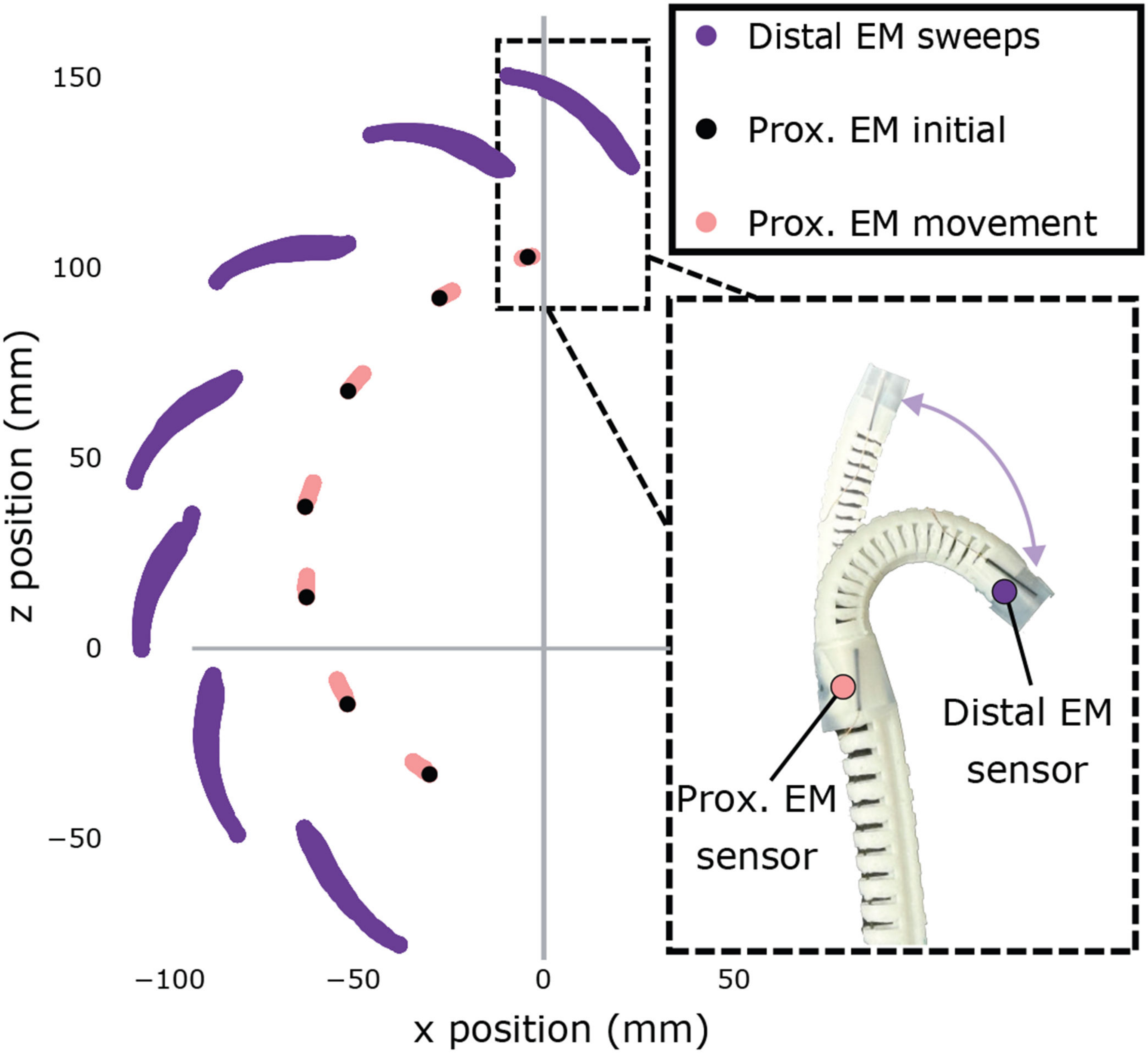

Fig. 8.

The independence between the distal and proximal notched continuum segments was shown by fully articulating the distal notched segment (purple) and measuring the movement at the end of the proximal notched segment (red) from its original position. This process was repeated at seven different starting positions throughout the workspace and showed that the two notched segments can be actuated relatively independently.

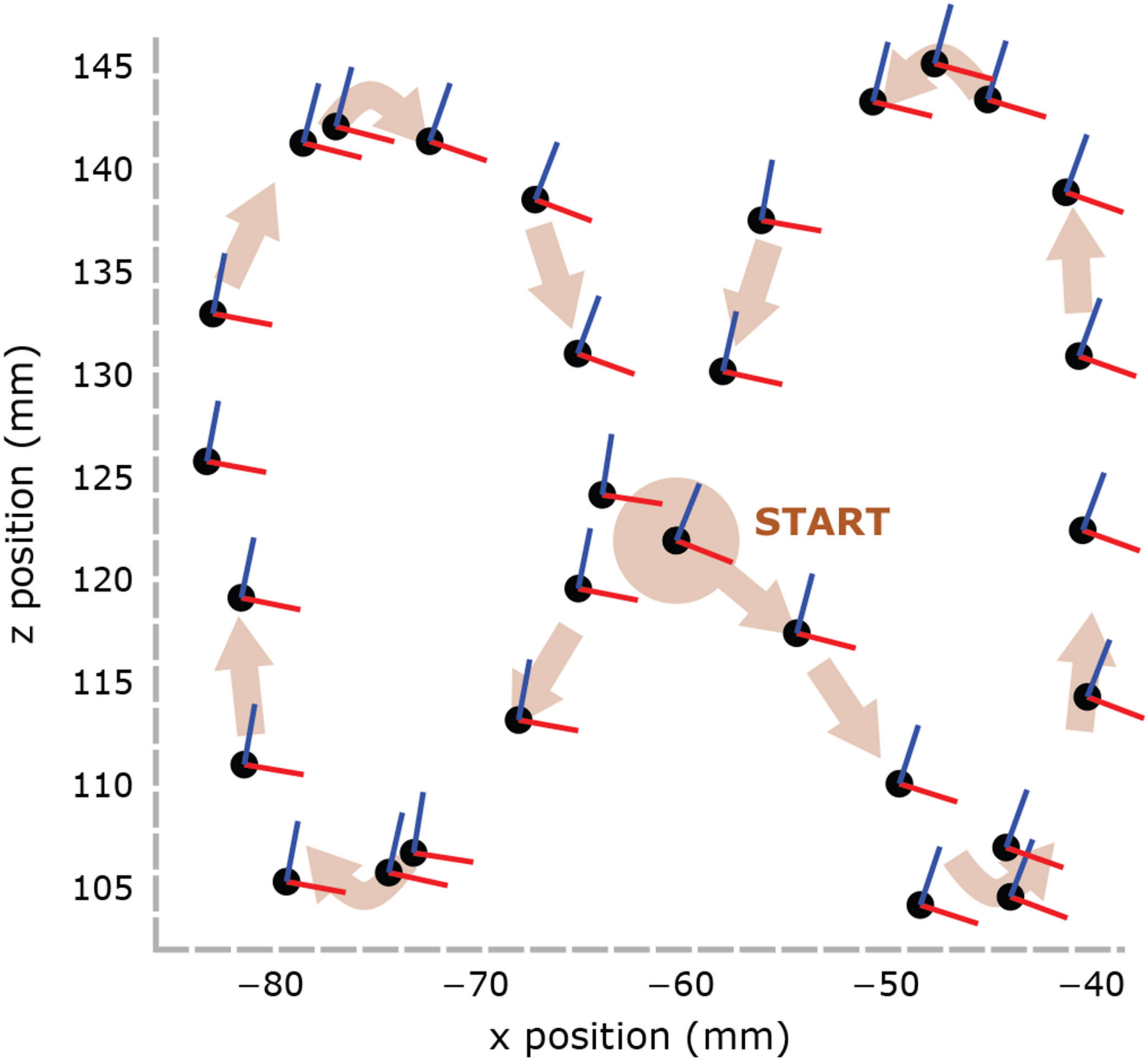

Fig. 9.

Commanding a change in position while maintaining orientation of the end effector. The path was a Lissajous pattern (similar to infinity symbol), showing that the position of soft growing robot deployment can be controlled while maintaining its deployment angle.

Fig. 10.

For three starting positions (I, II, and III), we commanded the notched continuum robot tip to rotate while maintaining position. For position I (green), the conceptual backbone shows the initial configuration in which the soft growing robot would deploy down and to the left. The max rotation configuration shows how the curvature of the notched continuum segments and system insertion (purple) updated to maintain tip position but change deployment orientation (up the ICA). The total commanded angle for all positions was based on the initial configuration and was broken up into 10 poses. Each tip position had three trials, for a total of nine tests which validated the inverse kinematic mapping.

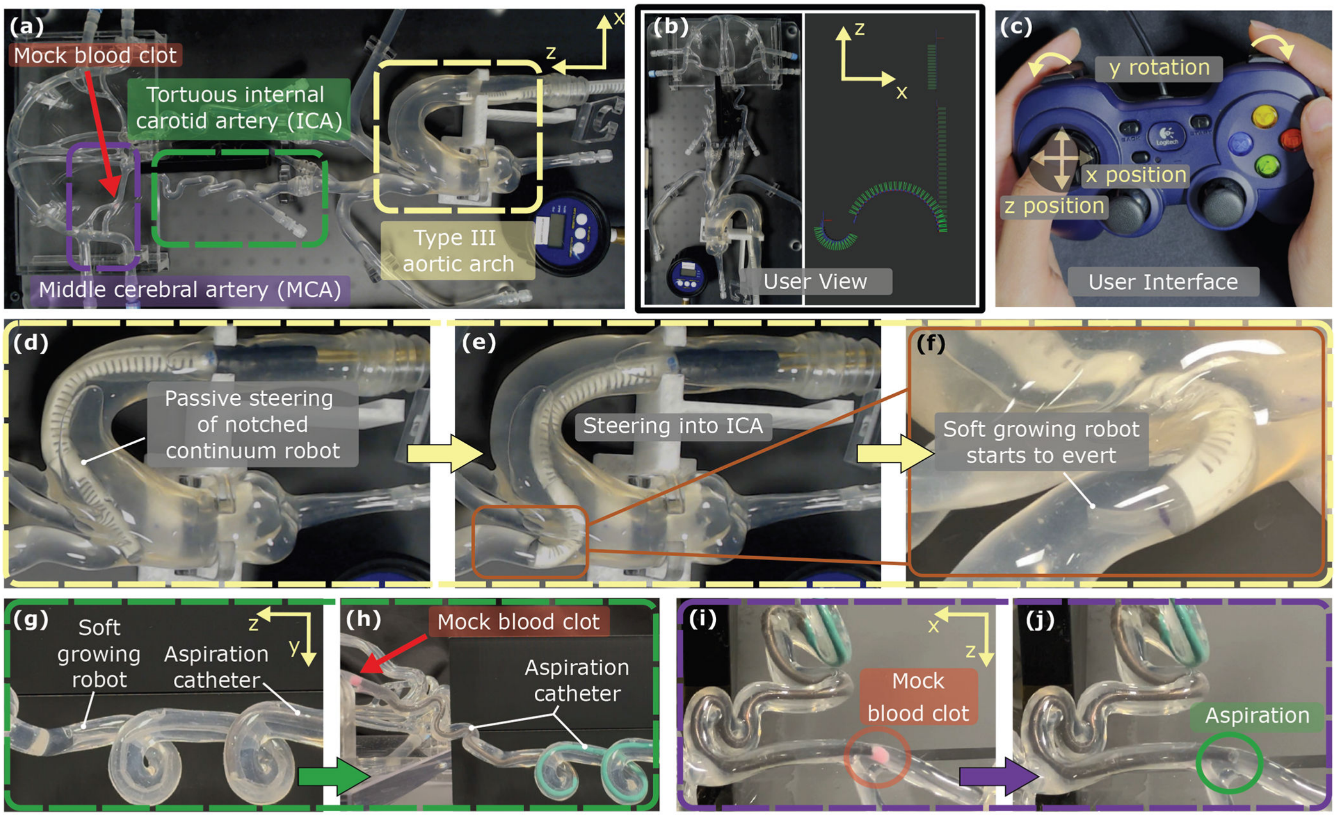

Fig. 11.

Full system deployment in the (a) benchtop endovascular model with a type III aortic arch, highly tortuous ICA, and mock blood clot in the MCA. (b) User view which simulated planar fluoroscopy available during a mechanical thrombectomy and a Rviz representation of the notched continuum robot. (c) The user interface which allowed for steering tip position in task space as well as actuate individual joints. (f) Passively conforming to environment before (e) steering into the origin of the ICA, and (f) deploying a soft growing robot. (g) The soft growing robot pulling the aspiration catheter up the tortuous ICA — comprising two 360-degree loops with 7.3 mm radius of curvature, two 180-degree bends with 6.2 and 4.2 mm radii of curvature, and a 4.6 mm siphon bend before MCA — until (h) the aspiration catheter (5F SOFIA) reaches the mock blood clot in the MCA. The SOFIA catheter has a more flexible distal end (dark gray) than proximal (green), but it is all composed within one piece. (i) View of the aspiration catheter reaching the pink mock blood clot and (j) successful aspiration with disappearance of the pink mock blood clot. The soft growing robot was then retracted followed by the soft notched continuum robot and can be seen along with the entire full system experiment in Supplementary Video S1.

TABLE I

NOTCHED CONTINUUM ROBOT PARAMETERS

Symbol	Def.	Proximal	Distal
g	Notch depth	5.0 mm	5.0 mm *
h	Notch height	1.7 (1.09) mm	1.43 (0.82) mm *
c	Uncut height	2.0 (2.61) mm	1.07 (1.68) mm
n	Number of notches	27	15
r_i	Inner radius of tube	3.0 mm	3.0 mm
r_o	Outer radius of tube	3.8 mm	3.8 mm
E	Young’s Modulus	Not used	7.8 MPa
t_{dia}	Tendon diameter	Not used	0.37 mm
$\overline{y}$	Neutral axis location	Eq. (6)	Eq. (2)
ε	Strain	Not used	Eq. (3)
F_{tendon}	Actuation force	Not used	Eq. (4)

”*” indicates output of optimization in Section III-B

”( )” parentheses indicate the measured value